NANO LETTERS

pubs.acs.org/NanoLett

Letter

Screening of Excitons by Organic Cations in Quasi-Two-Dimensional Organic–Inorganic Lead-Halide Perovskites

Marina R. Filip,* Diana Y. Qiu, Mauro Del Ben, and Jeffrey B. Neaton*

Cite This: *Nano Lett.* 2022, 22, 4870–4878

Read Online

ACCESS | Metrics & More | Article Recommendations | Supporting Information

ABSTRACT: Interlayer organic cations in quasi-two-dimensional halide perovskites are a versatile tuning vehicle for the optoelectronic properties of these complex systems, but chemical intuition for this design route is yet to be established. Here, we use density functional theory, the *GW* approximation, and the Bethe-Salpeter equation approach to understand the contribution of the organic cation to the quasiparticle band gap and exciton binding energy of layered perovskites. We show that organic cations in quasi-two-dimensional perovskites contribute significantly to the dielectric screening in these systems, countering quantum confinement effects on the quasiparticle band gap and the exciton binding energy. Using a simple electrostatics model inspired by parallel-plate capacitors, we decouple the organic cation and inorganic layer contributions to the effective dielectric constants and show that dielectric properties of layered perovskites are broadly tunable via the interlayer cation, providing a direct means of tuning photophysical properties for a variety of applications.

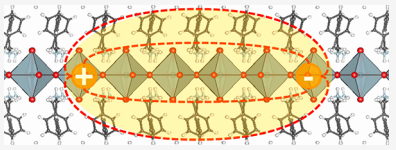

KEYWORDS: *layered perovskites, excitons, screening, halide perovskites, quantum confinement, optical properties*

Layered hybrid organic–inorganic metal-halide perovskites are a highly promising family of quasi-low-dimensional heterogeneous semiconductors for optoelectronic applications.[1−8] These materials are generally highly stable in ambient conditions and can be flexibly synthesized in bulk form,[4,6] exfoliated to a monolayer,[9] assembled in interfaces with transition metal dichalcogenides[10,11] or other layered perovskites,[12,13] or self-assembled in perovskite-nonperovskite single-crystal heterostructures.[14] The structural and chemical versatility of layered perovskites is in large part due to the wide range of organic cations that may be incorporated between the perovskite layers.[8] However, this highly attractive feature significantly enhances their structural and chemical complexity and poses great challenges for the fundamental study of their optoelectronic properties.

Layered lead-halide perovskites can be thought of as derivative structures of the three-dimensional (3D) halide perovskites (e.g., $CH_3NH_3PbI_3$[15,16]). Depending on the size, shape, and charge of the organic cation, layered perovskites can arrange in either flat layers of corner-sharing inorganic octahedra, more complex corrugated layers, or layers which include both corner and face-sharing octahedra.[4,6,8,14] Ruddlesden–Popper (RP) perovskites have a standard chemical formula of $A'_{n-1}A_2B_nX_{3n+1}$, where A and A′ are monovalent cations, B is a divalent metal cation, X is a halogen anion, and n is the number of BX_6 octahedra stacked up in a single layer.[4] In the n = 1 limit, RP perovskites have a chemical formula of A_2BX_4 and exhibit an effectively 2D behavior, with electronic coupling between layers suppressed by organic cations.[17] Quantum confinement effects in this case increase the quasiparticle band gap by more than 1 eV and the exciton binding energy by up to a factor of 10, as compared to 3D perovskite counterparts.[3] By increasing n from the quasi-2D limit (n = 1) toward bulk (n = ∞), quantum confinement effects are gradually reduced, and the optical absorption onset and exciton binding energies are red-shifted.[18,19]

The optoelectronic properties of A_2BX_4-type perovskites are highly tunable via partial or total chemical substitution of the A, B, and X components, in close similarity to their 3D counterparts.[20−29] The optical spectrum blue shifts with decreasing X anion[30] and red shifts from Pb to Sn.[31] As in 3D perovskites, the A-site cations do not contribute directly to optical transitions close to the onset.[29] Furthermore, as in 3D perovskites,[29,32−36] A-site cations in layered perovskites induce structural changes on the inorganic octahedral network, which, in turn, modulate the quasiparticle band gap and charge carrier effective masses.[30,37,38] In contrast, while the A-site cation does not significantly impact the high frequency dielectric constant of 3D halide perovskites,[39,40] and implicitly the binding energy of photoexcited charge carriers,[34,35] experimental reports suggest that altering the organic cations in layered perovskites may reduce the exciton binding energy by up to 300 meV.[41−44]

Advances in density functional theory (DFT)[45] and *ab initio* many-body perturbation theory (MBPT)[46,47] within the *GW* approximation[48] for single-particle excitations and the Bethe-Salpeter equation (BSE)[49,50] approach for neutral two-particle

Received: March 31, 2022
Revised: May 5, 2022
Published: June 9, 2022

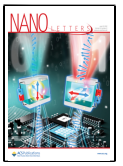

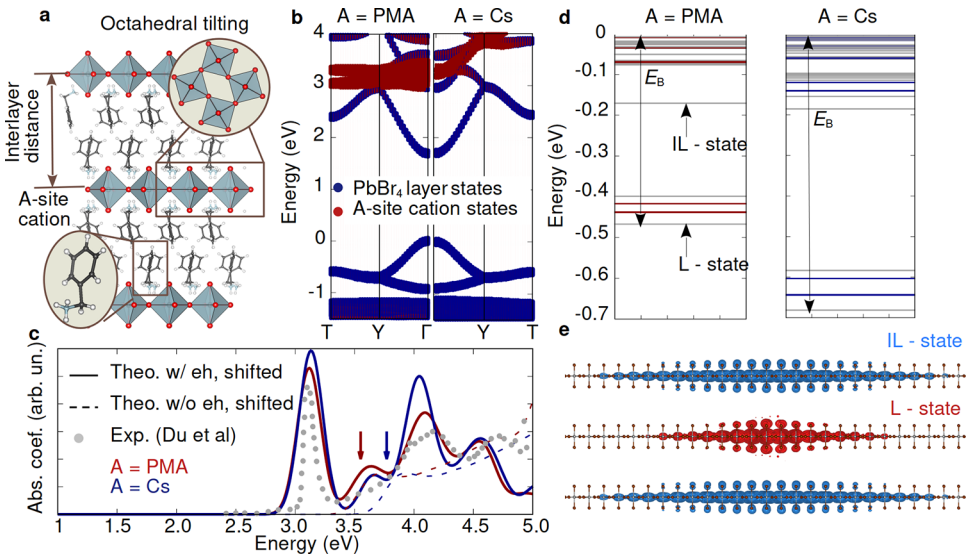

Figure 1. Summary of our DFT and *GW*+BSE calculations for PMA_2PbBr_4. **a.** Polyhedral model of the experimental PMA_2PbBr_4 reported in ref 30. **b.** Electronic band structure and projected density of states calculated within DFT/PBE including spin−orbit coupling for PMA_2PbBr_4 (left panel) and $Cs_2^{PMA}PbBr_4$ (right panel). The zero of energy is set to the valence band edge. **c.** Optical absorption spectra calculated within the independent particle approximation (dotted lines) and the BSE (continuous lines) calculated for PMA_2PbBr_4 (dark red) and $Cs_2^{PMA}PbBr_4$ (dark blue). Both optical absorption spectra are blue-shifted by 0.6 eV in order to match the onset of the experimental optical absorption spectra (gray disks) reported in ref 30. **d.** Energies of bound neutral excitations in PMA_2PbBr_4 (left panel) and $Cs_2^{PMA}PbBr_4$ (right panel). Bright states are represented with dark red (blue), and dark states are represented in gray. The zero energy level is set to the quasiparticle band gap. Labels "L" and "IL" refer to layer and interlayer states, respectively. **e.** Electron localization probability corresponding to the lowest excited state (L-state) and the ninth excited state (IL-state) when the hole is fixed on a Pb atom in the middle perovskite layer for PMA_2PbBr_4.

excitations have enabled this framework to be successfully employed to study materials with increasing degrees of complexity, such as bulk and monolayers of transition metal dichalcogenides,[51−53] organic semiconductors,[54] and heterogeneous metal-halide perovskites.[39,55−57] Prior *ab initio* calculations of the electronic structure of layered perovskites have so far been largely focused on understanding dielectric and quantum confinement effects driven by the inorganic layer thickness,[58,59] shape,[17,60] and the organic layer[18] and limited to standard DFT approaches. Due to the structural complexity of layered halide perovskites, *GW*+BSE methods have only been employed in two prior studies focusing on understanding the optical spectra and exciton binding energy in RP perovskites with n = 1, 2[61] and a model lead-halide perovskite monolayer with A = Cs.[62] In addition, ref 63 used a tight-binding *GW* +BSE approach to calculate the exciton binding energies of RP perovskites with n up to 5, highlighting the nonhydrogenic nature of excitons in these compounds.

In this work, we perform *GW*+BSE calculations to understand the contribution from organic cations to screening photogenerated electron−hole pairs in three RP lead-bromide perovskite semiconductors with n = 1, BA_2PbBr_4 (BA = butylammonium), PMA_2PbBr_4 (PMA = phenylmethylammonium), and NMA_2PbBr_4 (NMA = naphthalenemethylammonium). We show that unlike in 3D perovskites, the organic cation makes a nontrivial contribution to the high frequency dielectric screening, which impacts both the quasiparticle band gap and the exciton binding energy. We quantify this contribution using a simple electrostatic model inspired by standard formulas for parallel and series capacitors and consistent with prior literature.[41,64] We use this model to reveal how the organic cation can be designed to increase the effective dielectric constant of the layered perovskite, either by increasing the effective dielectric constant of the cation layer itself or by reducing the distance between the inorganic layers.

We start our study with PMA_2PbBr_4. In Figure 1b, we show the electronic band structure calculated using the Quantum Espresso code[65,66] and the Perdew-Burke-Erzerhof parametrization of the generalized gradient approximation (DFT/PBE)[67] including spin−orbit coupling (SOC),[91,92] for the experimental crystal structure of PMA_2PbBr_4 as reported in ref 30 (see the SI for details). PMA_2PbBr_4 has a direct band gap at Γ, and PMA cations contribute to bands more than 1 eV away from the conduction and valence band edge states (see Figure 1b), in line with previous DFT calculations.[17,19] Therefore, one could naively exclude any association of interlayer organic cations with the optical absorption onset of these systems.

We calculate electronic and optical excitations of PMA_2PbBr_4 within the *GW*+BSE framework, as implemented in the BerkeleyGW code[68−70] (see the SI for computational details and convergence studies). Using a "single-shot" G_0W_0 approach, employing the Godby-Needs plasmon-pole model and the static remainder approximation[93,94], and starting from DFT/PBE including SOC, we find a quasiparticle band gap of 3 eV. In Figure 1b, we show the *GW*+BSE optical absorption spectrum, in comparison with the independent particle spectrum and with experiment. The optical spectrum exhibits a sharp peak at the onset of absorption, 467 meV below the quasiparticle band gap, reflecting strong electron−hole interactions. The line shape of our calculated optical absorption spectrum, which includes an empirical 0.1 eV broadening, is in very good agreement with experimental data reported in ref 30, as shown in Figure 1c. However, the position of the main excitonic peak is red-shifted with respect to experiment by 0.6 eV; this discrepancy is in line with previous G_0W_0 calculations reported for 3D perovskites and has been associated with the G_0W_0 starting-point dependence,

https://doi.org/10.1021/acs.nanolett.2c01306
Nano Lett. 2022, 22, 4870−4878

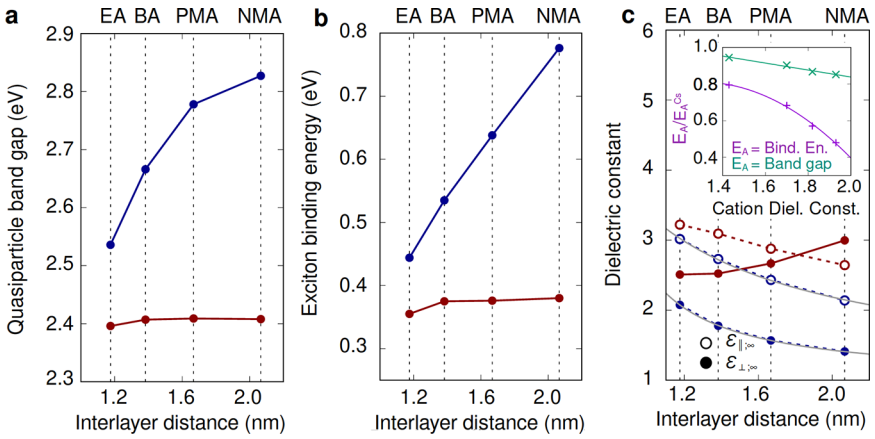

Figure 2. Quasiparticle band gaps (a), exciton binding energies (b), and optical dielectric constants for the in- and out-of-plane polarization directions (c) calculated within the *GW*+BSE framework for model structures without octahedral tilting including organic cations EA, BA, PMA, and NMA (dark red data points) and with Cs replacing the organic cations for the same interlayer distance (dark blue data points). The dark blue and dark red lines in all plots are guides to the eye. The gray lines in (c) correspond to fits of the dielectric constants as a function of the interlayer distance, as described in the main text and SI. The inset of (c) depicts the dependence of the fractional difference between the quasiparticle band gap and exciton binding energy on the cation dielectric constant calculated as described in the main text. The continuous lines in the inset correspond to quadratic and linear fits of the data, as discussed in the main text.

which can be partially resolved through self-consistency or using hybrid functional starting points.[71−75] In addition, our convergence studies predict a systematic underestimation of the band gap in the range of 0.1−0.2 eV (see the SI). To reduce computational effort, while capturing the physics, we restrict our level of theory for the quasiparticle energies to the single-shot G_0W_0@PBE approach and use empirical scissor corrections only to compare experimental and computed optical absorption spectra.

In Figure 1d, we show the fine structure of the computed bound excited states, i.e., those below the quasiparticle band gap; of main interest are the first 16 excited states which correspond to transitions between the 4 degenerate conduction and valence band edge states. The first 8 states are grouped in the lower energy region between −0.5 eV and −0.4 eV and correspond to excitons localized within the $PbBr_4$ perovskite layer (shown in Figure 1e); we label this group of states with L. These states include three transitions which are optically inactive (dark), and five which are optically active (bright) and contribute to the main excitonic peak of the optical absorption spectra (Figure 1c). The lowest excited state is dark, with an energy approximately 30 meV below the second highest bright state, in very good agreement with the measured fine structure of closely related PEA_2PbBr_4 (PEA = phenylethylammonium).[76] Four of the five bright states are nearly degenerate and optically active for a light polarization direction along the $PbBr_4$ plane, while the fifth one (23 meV above) is optically active for light polarized in the direction perpendicular to the $PbBr_4$ layer; this is consistent with recent experiments reporting the occurrence of bright in- and out-of-plane excitons in RP perovskites.[64,76−78] The 8 states in the second group, occurring just above −0.2 eV (Figure 1d), are all nearly degenerate and dark; in these states, photoexcited electrons are localized in a different layer from the holes (An example of one of the eight states is shown in Figure 1e.), and we label these with IL.

Next, we probe the contribution of the PMA cation layer to computed excitons described above by investigating how these properties change in a fictitious scenario when the organic cation, PMA, is replaced by a monatomic cation, Cs, without changing the structure of the $PbBr_4$ octahedral layers; this structure is labeled as $Cs_2^{PMA}PbBr_4$. As expected, the DFT-PBE band structure of $Cs_2^{PMA}PbBr_4$ displays nearly identical band edges to PMA_2PbBr_4, since the A-site cations do not contribute directly to these states. Furthermore, optical spectra for $Cs_2^{PMA}PbBr_4$ and PMA_2PbBr_4 have onsets at very close energies. The quasiparticle band gap and exciton binding energy of $Cs_2^{PMA}PbBr_4$ are blue-shifted with respect to PMA_2PbBr_4 by 0.2 eV, while the order of the first 16 excited states states discussed above remains qualitatively similar. The difference in the exciton binding energies computed in the two cases correlates with the dielectric constants of the two model layered perovskites (2.8 for PMA vs 2.4 for Cs^{PMA}), and the ratio of the binding energies (0.69) is very close to the squared inverse ratio of the high frequency dielectric constants, 0.73, as expected from the hydrogenic model.[79] This contribution from the PMA cation is in stark contrast to 3D halide perovskites.[35] It is important to note that our focus in this analysis is on the high frequency (electronic) dielectric screening, and all our calculations ignore the contribution to screening arising from phonons, which has been recently shown to reduce exciton binding energies of semiconductors and insulators by up to 50%,[39] when the exciton binding energies and the LO phonon energies have similar energies. In n = 1 Ruddlesden−Popper perovskites, exciton binding energies can reach values up to 10−20 times larger than characteristic phonon frequencies,[80] suggesting that the phonon contribution to screening is negligible in this case.

Figure 1 and the arguments above strongly suggest that organic cation layers are important contributors to the dielectric screening of excitations in layered perovskites. To understand this contribution, we perform a systematic analysis of layered perovskites with A-site cations of different sizes and shapes: ethylammonium (EA), butylammonium (BA), phenylmethylammonium (PMA), and naphthalenemethylammonium (NMA). The size of the organic cation determines the interlayer distance, d, between the $PbBr_4$ layers and the degree of octahedral tilting within each layer, two structural parameters that are expected to impact optoelectronic properties.[30,81] In the following, we will study the influence

https://doi.org/10.1021/acs.nanolett.2c01306
Nano Lett. 2022, 22, 4870−4878

Table 1. Cation Layer Dielectric Constants Calculated Using the Dielectric Model Described in the Main Text and the SI (Columns 2−4), and the Clausius-Mosotti Relation (Column 5)

component	$\varepsilon_{\perp}^{\infty}$	$\varepsilon_{\parallel}^{\infty}$	$\varepsilon_{ave}^{\infty}$	$\varepsilon_{ave;CM}^{\infty}$
EA	1.27	1.52	1.43	1.74
BA	1.53	1.79	1.70	1.94
PMA	1.86	1.81	1.82	2.11
NMA	2.36	1.76	1.93	2.40
inorganic layer	5.81	4.22	4.64	N/A

of both of these parameters separately, using model and experimental layered perovskite structures.

We first analyze the role of interlayer separation exclusively, by constructing a set of model structures with undistorted $PbBr_4$ layers (Pb-Br bond length of 2.937 Å, as in Ref. 95) which do not exhibit any octahedral tilting, and are separated by inter-layer distances reported in Refs. 30 and 81 and Ref. 3 (see the SI for details); we compare calculations performed on these model structures constructed with the organic cation and with Cs. For this analysis, we perform *GW*+BSE calculations for 8 distinct structures (see the SI for details). As in Figure 1, DFT/PBE band gaps are independent of the interlayer distance or the A-site cation type (see Table S1 of the SI). Similarly, G_0W_0 quasiparticle band gaps and *GW*+BSE exciton binding energies vary by less than 50 meV across the five model structures with different organic A-site cations. On the other hand, upon replacement of the organic A-site cation by Cs, our calculated quasiparticle band gaps increase with an increasing interlayer distance over a range of up to 0.3 eV, as shown in Figure 2a, and exciton binding energies follow the same trend spanning a range of up to 0.4 eV (Figure 2b).

The large difference between band gaps and exciton binding energies for structures with and without the organic cations can be explained from a comparison of the dielectric constants of the two types of structures (Figure 2c). In Figure 2c, we plot both the in-plane and out-of-plane polarization directions, $\varepsilon_{\parallel}^{\infty}$ and $\varepsilon_{\perp}^{\infty}$, respectively, in order to account for the anisotropy of these systems. In all cases, the A-site cation layer contributes to an increase in the dielectric constants (both in- and out-of-plane) by up to a factor of 2, with the contribution increasing as the interlayer distance increases, thereby reducing the quasiparticle band gap and the exciton binding energies.

The dielectric constants shown in Figure 2c include a contribution from the inorganic layer $\varepsilon_{\parallel(\perp)}^{\infty;L}$ and the organic cation layer $\varepsilon_{\parallel(\perp)}^{\infty;A}$. To decouple these contributions from the bulk dielectric constant we calculated within the random phase approximation (RPA),[84,85] we develop a simple model for the effective dielectric constant, inspired from the elementary formulas for in-series and in-parallel capacitors, equivalent to previous approaches described in the literature[41,64] (see the SI for details). We first extract the dielectric constantand thickness (d_L) of the $PbBr_4$ layer , and the dielectric constant of the cation layer by fitting the model expressions to the dielectric constants obtained for the Cs-based model structures to obtain d_L = 7.41 Å (close to the width of a $PbBr_4$ octahedron of 5.9 Å), $\varepsilon_{\perp}^{\infty;L}$ = 5.81 and $\varepsilon_{\parallel}^{\infty;L}$ = 4.22 (consistent with 3D lead-bromide perovskites[39]), and $\varepsilon_{\perp(\parallel)}^{\infty;A} \sim 0.99$ (consistent with vacuum permittivity).

Using this simple model, we extract the dielectric constants corresponding to the layers with different cation species given in Table 1. The ratio of exciton binding energies and quasiparticle band gaps calculated for structures with and without organic cations correlates quadratically and linearly with the average dielectric constant of the organic cation layer, respectively, consistent with the assumption that organic cations screen charge carriers in layered halide perovskites (see the inset of Figure 2c). Interestingly, the dielectric constants of the organic cation layers calculated with this fitting procedure follow a very similar trend to those calculated

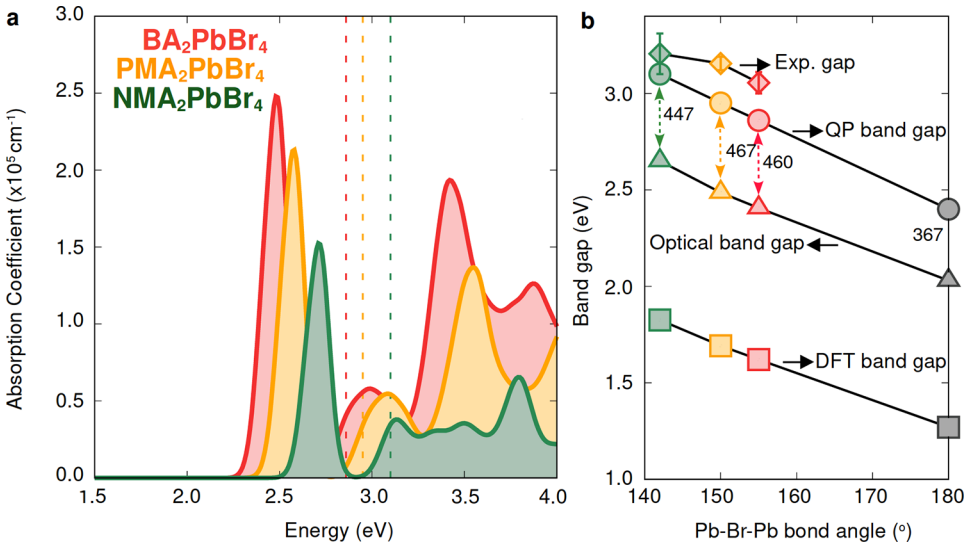

Figure 3. (a) Optical absorption spectra calculated for the experimental structures of BA_2PbBr_4 (red), PMA_2PbBr_4 (yellow), and NMA_2PbBr_4 (green) as described in detail in the SI within the *GW*+BSE approach. Dotted lines mark the quasiparticle band gaps in each case. (b) Comparison between the mean field DFT, optical, quasiparticle, and experimental band gaps for BA_2PbBr_4 (red), PMA_2PbBr_4 (yellow), and NMA_2PbBr_4 (green) and the band gaps calculated for the model untilted layered perovskites (gray data points). The band gaps corresponding to the model layered perovskites are obtained as an average of the band gaps shown in Figure 2. Experimental optical band gaps are read from the positions of the main excitonic peaks in the optical absorption spectra measured at room temperature, as reported in ref 96 for BA_2PbBr_4 and ref 30 for PMA_2PbBr_4 and averaged over values from refs 30 and 87 for NMA_2PbBr_4.

https://doi.org/10.1021/acs.nanolett.2c01306
Nano Lett. 2022, 22, 4870−4878

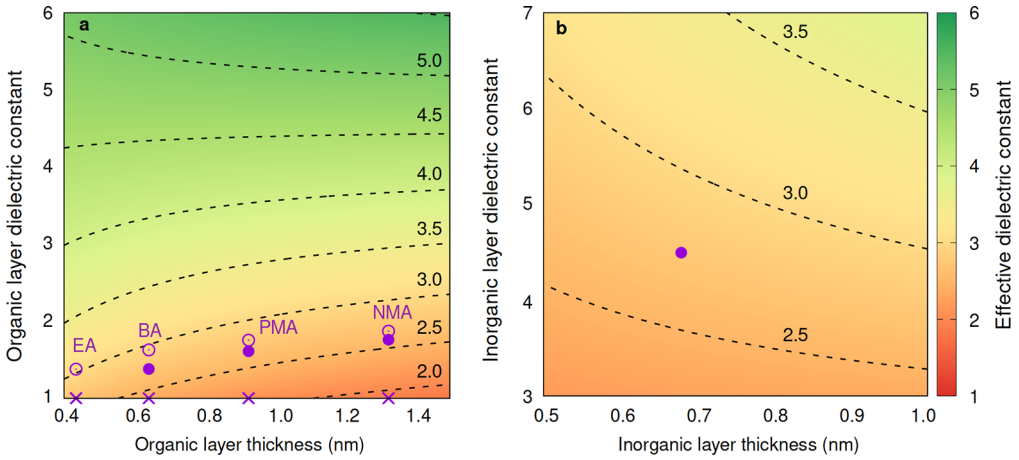

Figure 4. (a) Effective dielectric constant of a hypothetical lead-bromide layered perovskite with the width of the inorganic layer, d_L = 7.41 Å, and the average dielectric constant of the inorganic layer, $\varepsilon_{ave}^{\infty;L}$ = 4.64, as a function of the width and dielectric constant of the organic layer. The empty circles correspond to calculated values of the model EA_2PbBr_4, BA_2PbBr_4, PMA_2PbBr_4, and NMA_2PbBr_4, and the filled disk corresponds to calculated values for the experimental structures of the latter three layered perovskites. The points marked by crosses correspond to dielectric constants calculated for model structures in which the organic cation is replaced by Cs. (b) Effective dielectric constant of a hypothetical layered perovskite with PMA as the organic layer, as a function of the inorganic layer thickness and dielectric constant. The purple disk corresponds to the case of PMA_2PbBr_4 ($\varepsilon_{ave}^{\infty;A}$ = 1.82 and an inorganic layer thickness of 7.41 Å). The effective dielectric constant in both (a) and (b) is defined as $\varepsilon_{eff}^{-1} = (2\varepsilon_{\parallel}^{-1} + \varepsilon_{\perp}^{-1})/3$, and we assume that dielectric constants of the organic and inorganic layers are isotropic ($\varepsilon_{\parallel}^{\infty;A(L)} \sim \varepsilon_{\perp}^{\infty;A(L)} \sim \varepsilon_{ave}^{\infty;A(L)}$).

using the Clausius−Mosotti relation[86] and molecular polarizabilities calculated within the time-dependent density functional perturbation theory framework (TD-DFPT),[82,83] at the RPA level. The Clausius−Mosotti dielectric constants consistently overestimate first-principles results; we tentatively assign this difference to the absence of effects emerging from small intermolecular interactions or to inaccuracies in estimating the organic layer volume (which does not take into account interpenetration between the inorganic and organic layers). Despite this systematic discrepancy, the agreement between the two independently calculated trends suggests that it may be possible to estimate dielectric constants for the organic cation layers without the need for computationally demanding *GW* calculations.

In Figure 3a, we show optical spectra calculated within the *GW*+BSE approach for experimental structures of BA_2PbBr_4, PMA_2PbBr_4, and NMA_2PbBr_4, (see SI for details. 93) which exhibit increasing Pb−Br−Pb bond angles as the cation size increases (see Figure 3b). Unlike the model case, excitonic peaks blue shift as the size of the cation increases. The same trend is followed by the band gaps (both from DFT-PBE and G_0W_0), with an almost linear correlation with the magnitude of the in-plane Pb−Br−Pb bond angles, in very good agreement with previous computational studies of layered perovskites,[88] three-dimensional perovskites,[29,89] and experiment (Figure 2b). In close agreement with Figure 2b, we find that the exciton binding energy is largely independent of the cation type for the three experimental structures analyzed here. Furthermore, exciton binding energies are systematically 20% larger than those obtained for the model structures, in part due to the increase in charge carrier effective masses with increasing octahedral tilting; this effect has been explicitly computed in previous studies both for 3D perovskites[29,89] as well as in layered perovskites.[36]

Finally, we return to the dielectric model of Figure 2c to illustrate how the choice of the organic cation can tune the dielectric properties of layered perovskites. In Figure 4, we visualize the dependence of the effective dielectric constant in two cases: (i) with d_L = 7.41 Å and $\varepsilon_{ave}^{\infty;L}$ = 4.64 fixed and (ii) with d_A = 9.26 Å and $\varepsilon_{ave}^{\infty;A}$ = 1.82 (PMA) fixed. The most effective route to tuning the effective dielectric constant, according to our model, is by modifying the dielectric constant of the organic cation layer; this is in stark contrast to 3D perovskites. For example, doubling the dielectric constant of the PMA layer could increase the effective dielectric constant of a layered perovskite by up to 50% without changing the inorganic layer chemistry. By contrast, scanning through expected dielectric constants of inorganic layers (corresponding to chloride, bromide, and iodide perovskites) we find that the effective dielectric constants are much less sensitive to the dielectric properties and size of the inorganic layer. This indicates that the exciton binding energies of layered perovskites with different halogen compositions should be mostly dictated by the curvature of the conduction and valence band edges and less so by the dielectric properties of the inorganic layer. Our results are in line with recent experimental studies implementing cations which are highly polar,[43] including heavier ions[44] or including two ammonium groups;[90] refs 43 and 44 report a significant reduction in the exciton binding energy, as qualitatively predicted by the simple model depicted in Figure 4.

In conclusion, we have presented a comprehensive first-principles analysis of the optoelectronic properties of several organic−inorganic Ruddlesden−Popper layered lead-halide perovskites. We have shown that unlike their three-dimensional counterparts, in layered perovskites the organic cations play a key role in the optical properties of these materials, through contributions to the dielectric screening of photogenerated carriers within the layers. Using a set of simplified model structures, we have quantified this contribution, calculated the dielectric constant corresponding to the organic cation layer, and shown that dielectric screening originating with the organic cation counterbalances quantum confinement effects and acts to reduce the exciton binding energy as compared to inorganic monocations. This intuition was confirmed by calculations for experimental structures of

https://doi.org/10.1021/acs.nanolett.2c01306
Nano Lett. 2022, 22, 4870−4878

BA_2PbBr_4, PMA_2PbBr_4, and NMA_2PbBr_4, which showed that octahedral tilting mainly contributes to shift the position of the optical absorption onset but does not impact the dielectric properties of layered perovskites significantly. Finally, we used a simple model to predict that the effective dielectric constant of layered perovskites can be significantly enhanced by increasing the dielectric constant of the organic cation or decreasing the distance between the inorganic layers. Thereby, the interlayer organic cations could potentially facilitate the reduction of exciton binding energies more efficiently than the chemical composition of the inorganic layers, as previously expected from their 3D counterparts. The chemical intuition outlined in this work can provide a reliable pathway toward the development of efficient optoelectronic devices implementing layered hybrid organic−inorganic halide perovskites.

■ ASSOCIATED CONTENT

Supporting Information

The Supporting Information is available free of charge at https://pubs.acs.org/doi/10.1021/acs.nanolett.2c01306.

Computational and model details, as well as convergence tests and additional references (PDF)

■ AUTHOR INFORMATION

Corresponding Authors

Marina R. Filip − *Department of Physics, University of Oxford, Clarendon Laboratory, Oxford OX1 3PU, United Kingdom;* orcid.org/0000-0003-2925-172X; Email: marina.filip@physics.ox.ac.uk

Jeffrey B. Neaton − *Department of Physics, University of California, Berkeley, California 94720, United States; Materials Science Division, Lawrence Berkeley National Laboratory, Berkeley, California 94720, United States; Kavli Energy Nano Sciences Institute at Berkeley, Berkeley, California 94720, United States;* Email: jbneaton@lbl.gov

Authors

Diana Y. Qiu − *School of Engineering and Applied Science, Yale University, New Haven, Connecticut 06511, United States;* orcid.org/0000-0003-3067-6987

Mauro Del Ben − *Computational Science Division, Lawrence Berkeley National Laboratory, Berkeley, California 94720, United States*

Complete contact information is available at: https://pubs.acs.org/10.1021/acs.nanolett.2c01306

Notes

The authors declare no competing financial interest.

■ ACKNOWLEDGMENTS

This work received support from the Center for Computational Study of Excited-State Phenomena in Energy Materials (C2SEPEM) at the Lawrence Berkeley National Laboratory, funded by the U.S. Department of Energy, Office of Science, Basic Energy Sciences, Materials Sciences and Engineering Division, under Contract No. DE-C02-05CH11231. M.R.F. acknowledges support from the UK Engineering and Physical Sciences Research Council (EPSRC), grant no. EP/V010840/1, the John Fell Oxford University Press (OUP) Research Fund, and the Molecular Foundry user program, supported by the Office of Science, Office of Basic Energy Sciences, of the US DOE under contract DE-AC02-5CH11231. The authors acknowledge computational resources from Cori at the National Energy Research Scientific Computing Center (NERSC) and Summit at the Oak Ridge Leadership Computing Facility (accessed through the INCITE program, a DOE Office of Science User Facility; grant number DE-AC05-00OR22725). M.R.F., D.Y.Q., and M.D.B. acknowledge PRACE for awarding access to the Marconi100 supercomputer at CINECA, Italy.

■ REFERENCES

(1) Mitzi, D. B. Synthesis, Structure and Properties of Organic-Inorganic Perovskites and Related Materials. *Prog. Inorg. Chem.* **2007**, *48*, 1−121.

(2) Mitzi, D. B. Templating and Structural Engineering in Organic-Inorganic Perovskites. *J. Chem. Soc. Dalt. Trans.* **2001**, *1*, 1−12.

(3) Straus, D. B.; Kagan, C. R. Electrons, Excitons, and Phonons in Two-Dimensional Hybrid Perovskites: Connecting Structural, Optical, and Electronic Properties. *J. Phys. Chem. Lett.* **2018**, *9*, 1434−1447.

(4) Smith, M. D.; Crace, E. J.; Jaffe, A.; Karunadasa, H. I. The Diversity of Layered Halide Perovskites. *Annu. Rev. Mater. Res.* **2018**, *48*, 111−136.

(5) Connor, B. A.; Leppert, L.; Smith, M. D.; Neaton, J. B.; Karunadasa, H. I. Layered Halide Double Perovskites: Dimensional Reduction of Cs2AgBiBr6. *J. Am. Chem. Soc.* **2018**, *140*, 5235−5240.

(6) Smith, M. D.; Connor, B. A.; Karunadasa, H. I. Tuning the Luminescence of Layered Halide Perovskites. *Chem. Rev.* **2019**, *119*, 3104−3139.

(7) Connor, B. A.; Biega, R.-I.; Leppert, L.; Karunadasa, H. I. Dimensional reduction of the small-bandgap double perovskite Cs2AgTlBr6. *Chem. Sci.* **2020**, *11*, 7708−7715.

(8) Li, X.; Hoffman, J. M.; Kanatzidis, M. G. The 2D Halide Perovskite Rulebook: How the Spacer Influences Everything from the Structure to Optoelectronic Device Efficiency. *Chem. Rev.* **2021**, *121*, 2230−2291.

(9) Yaffe, O.; Chernikov, A.; Norman, Z. M.; Velauthapillai, A.; van der Zande, A.; Owen, J. S.; Heinz, T. F. Excitons in ultrathin organic-inorganic perovskite crystals. *Phys. Rev. B* **2015**, *92*, 045414.

(10) Chen, Y.; Liu, Z.; Li, J.; Cheng, X.; Ma, J.; Wang, H.; Li, D. Robust Interlayer Coupling in Two-Dimensional Perovskite/Monolayer Transition Metal Dichalcogenide Heterostructures. *ACS Nano* **2020**, *14*, 10258−10264.

(11) Zhang, Z.; Wang, S.; Liu, X.; Chen, Y.; Su, C.; Tang, Z.; Li, Y.; Xing, G. Metal-Halide Perovskite/2D Material Heterostructures: Syntheses and Applications. *Small Methods* **2021**, *5*, 2000937.

(12) Shi, E.; Yuan, B.; Shiring, S. B.; Gao, Y.; Akriti; Guo, Y.; Su, C.; Lai, M.; Yang, P.; Kong, J.; Savoie, B. M.; et al. Two-Dimensional Halide Perovskite Lateral Epitaxial Heterostructures. *Nature* **2020**, *580*, 614−620.

(13) Pan, D.; Fu, Y.; Spitha, N.; Zhao, Y.; Roy, C. R.; Morrow, D. J.; Kohler, D. D.; Wright, J. C.; Jin, S. Deterministic Fabrication of Arbitrary Vertical Heterostructures of Two-Dimensional Ruddlesden-Popper Halide Perovskites. *Nat. Nanotechnol.* **2021**, *16*, 159−165.

(14) Aubrey, M. L.; Valdes, A. S.; Filip, M. R.; Connor, B. A.; Lindquist, K. P.; Neaton, J. B.; Karunadasa, H. I. Directed Assembly of Layered Perovskite Heterostructures as Single Crystals. *Nature* **2021**, *597*, 355−359.

(15) Lee, M. M.; Teuscher, J.; Miyasaka, T.; Murakami, T. N.; Snaith, H. J. Efficient Hybrid Solar Cells Based on Meso-Superstructured Organometal Halide Perovskites. *Science* **2012**, *338*, 643.

(16) Kim, H.-S.; Lee, C.-R.; Im, J.-H; Moehl, T.; Marchioro, A.; Moon, S.-J.; Humphry-Baker, R.; Yum, J.-H.; Moser, J. E.; Grätzel, M.; et al. Lead Iodide Perovskite Sensitized All-Solid-State Submicron Thin Film Mesoscopic Solar Cell with Efficiency Exceeding 9%. *Sci. Reports* **2012**, *2*, 591.

(17) Kamminga, M. E.; Fang, H.-H.; Filip, M. R.; Giustino, F.; Baas, J.; Blake, G. R.; Loi, M. A.; Palstra, T. T. M. Confinement Effects in

Low-Dimensional Lead Iodide Perovskite Hybrids. *Chem. Mater.* **2016**, *28*, 4554−4562.
(18) Traore, B.; Pedesseau, A. L. L.; Che, X.; Blancon, J.-C.; Tsai, H.; Nie, W.; Stoumpos, C. C.; Kanatzidis, M. G.; Tretiak, S.; Mohite, A. D.; et al. Composite Nature of Layered hybrid Perovskites: Assessment on Quantum and Dielectric Confinements and Band Alignment. *ACS Nano* **2018**, *12*, 3321−3332.
(19) Even, J.; Pedesseau, L.; Katan, C. Understanding Quantum Confinement of Charge Carriers in Layered 2D Hybrid Perovskites. *ChemPhysChem* **2014**, *15*, 3733−3741.
(20) Hao, F.; Stoumpos, C. C.; Chang, R. P. H.; Kanatzidis, M. G. Anomalous Band Gap Behavior in Mixed Sn and Pb Perovskites Enables Broadening of Absorption Spectrum in Solar Cells. *J. Am. Chem. Soc.* **2014**, *136*, 8094−8099.
(21) Eperon, G. E.; Leijtens, T.; Bush, K. A.; Prasanna, R.; Green, T.; Wang, J. T.-W.; McMeekin, D. P.; Volonakis, G.; Milot, R. L.; May, R.; et al. Perovskite-perovskite tandem photovoltaics with optimized band gaps. *Science* **2016**, *354*, 861−865.
(22) Slavney, A. H.; Hu, T.; Lindenberg, A. M.; Karunadasa, H. I. A Bismuth-Halide Double Perovskite with Long Carrier Recombination Lifetime for Photovoltaic Applications. *J. Am. Chem. Soc.* **2016**, *138*, 2138−2141.
(23) McClure, E. T.; Ball, M. B.; Windl, W.; Woodward, P. M. Cs2AgBiX6 (X = Br, Cl): New Visible Light Absorbing, Lead-Free Halide Perovskite Semiconductors. *Chem. Mater.* **2016**, *28*, 1348−1354.
(24) Filip, M. R.; Hillman, S.; Haghighirad, A.-A.; Snaith, H. J.; Giustino, F. Band Gaps of the Lead-Free Halide Double Perovskites Cs2BiAgCl6 and Cs2BiAgBr6 from Theory and Experiment. *J. Phys. Chem. Lett.* **2016**, *7*, 2579−2585.
(25) Volonakis, G.; Filip, M. R.; Haghighirad, A. A.; Sakai, N.; Wenger, B.; Snaith, H. J.; Giustino, F. Lead-Free Halide Double Perovskites via Heterovalent Substitution of Noble Metals. *J. Phys. Chem. Lett.* **2016**, *7*, 1254−1259.
(26) Protesescu, L.; Yakunin, S.; Bodnarchuk, M. I.; Krieg, F.; Caputo, R.; Hendon, C. H.; Yang, R. X.; Walsh, A.; Kovalenko, M. V. Nanocrystals of Cesium Lead Halide Perovskites (CsPbX 3, X = Cl, Br, and I): Novel Optoelectronic Materials Showing -Bright Emission with Wide Color Gamut. *Nano Lett.* **2015**, *15*, 3692−3696.
(27) Pellet, N.; Gao, P.; Gregori, G.; Yang, T.-Y.; Nazeeruddin, M. K.; Maier, J.; Grtzel, M. Mixed-Organic-Cation Perovskite Photovoltaics for Enhanced Solar-Light Harvesting. *Angew. Chem.* **2014**, *53*, 3151−3157.
(28) Eperon, G. E.; Stranks, S. D.; Menelaou, C.; Johnston, M. B.; Herz, L. M.; Snaith, H. J. Formamidinium lead trihalide: a broadly tunable perovskite for efficient planar heterojunction solar. *Energy Environ. Sci.* **2014**, *7*, 982−988.
(29) Filip, M. R.; Eperon, G. E.; Snaith, H. J.; Giustino, F. Steric engineering of metal-halide perovskites with tunable optical band gaps. *Nat. Commun.* **2014**, *5*, 5757.
(30) Du, K.; Tu, Q.; Zhang, X.; Han, Q.; Liu, J.; Zauscher, S.; Mitzi, D. B. Two-Dimensional Lead(II) Halide-Based Hybrid Perovskites Templated by Acene Alkylamines: Crystal Structures, Optical Properties and Piezoelectricity. *Inorg. Chem.* **2017**, *56*, 9291−9302.
(31) Mitzi, D. B. Synthesis, Crystal Structure and Optical and Thermal Properties of $(C_4H_9NH_3)_2MI_4$ (M = Ge, Sn, Pb). *Chem. Mater.* **1996**, *8*, 791−800.
(32) Filip, M. R.; Verdi, C.; Giustino, F. GW Band Structures and Carrier Effective Masses of CH3NH3PbI3 and Hypothetical Perovskites of the Type APbI 3: A = NH 4, PH 4, AsH 4 and SbH 4. *J. Phys. Chem. C* **2015**, *119*, 25209−25219.
(33) Miyata, A.; Mitioglu, A.; Plochocka, P.; Portugall, O.; Wang, J. T.-W.; Stranks, S. D.; Snaith, H. J.; Nicholas, R. J. Direct measurement of the exciton binding energy and effective masses for charge carriers in organic-inorganic tri-halide perovskites. *Nat. Phys.* **2015**, *11*, 582−587.
(34) Yang, Z.; Surrente, A.; Galkowski, K.; Miyata, A.; Portugall, O.; Sutton, R. J.; Haghighirad, A. A.; Snaith, H. J.; Maude, D. K.; Plochocka, P.; et al. Impact of Halide Cage on the Electronic Properties of Fully Inorganic Cesium Lead Halide Peerovskites. *ACS Energy Lett.* **2017**, *2*, 1621−1627.
(35) Galkowski, K.; Mitioglu, A.; Miyata, A.; Plochocka, P.; Portugall, O.; Eperon, G. E.; Wang, J. T.-W.; Stergiopoulos, T.; Stranks, S. D.; Snaith, H. J.; et al. Determination of the Exciton Binding Energy and Effective Masses for Methylammonium and Formamidinium Lead Tri-Halide Perovskite Semiconductors. *Energy Environ. Sci.* **2016**, *9*, 962−970.
(36) Dyksik, M.; Duim, H.; Zhu, X.; Yang, Z.; Gen, M.; Kohama, Y.; Adjokatse, S.; Maude, D. K.; Loi, M. A.; Egger, D. A.; et al. Broad Tunability of Carrier Effective Masses in Two-Dimensional Halide Perovskites. *ACS Energy Lett.* **2020**, *5*, 3609−3616.
(37) Mauck, C. M.; France-Lanord, A.; Hernandez Oendra, A. C.; Dahod, N. S.; Grossman, J. C.; Tisdale, W. A. Inorganic Cage Motion Dominates Excited-State Dynamics in 2D-Layered Perovskites $(C_xH_{2x}+1NH_3PbI_4$ (x = 4 - 9). *J. Phys. Chem. C* **2019**, *123*, 27904−27916.
(38) Surrente, A.; Baranowski, M.; Plochocka, P. Perspective on the Physics of Two-Dimensional Perovskites in High Magnetic Fields. *Appl. Phys. Lett.* **2021**, *118*, 170501.
(39) Filip, M. R.; Haber, J. B.; Neaton, J. B. Phonon Screening of Excitons in Semiconductors: Halide Perovskites and Beyond. *Phys. Rev. Lett.* **2021**, *127*, 067401.
(40) Poncé, S.; Schlipf, M.; Giustino, F. Origin of Low Carrier Mobilities in Halide Perovskites. *ACS Energy Lett.* **2019**, *4*, 456−463.
(41) Hong, X.; Isihara, T.; Nurmikko, A. V. Dielectric Confinement Effect on Excitons in PbI_4-based Layered Semiconductors. *Phys. Rev. B* **1992**, *45*, 6961−6964.
(42) Smith, M. D.; Pedesseau, L.; Kepenekian, M.; Smith, I. C.; Katan, C.; Even, J.; Karunadasa, H. I. Decreasing the electronic confinement in layered perovskites through intercalation. *Chem. Sci.* **2017**, *8*, 1960−1968.
(43) Cheng, B.; Li, T.-Y.; Maity, P.; Wei, P.-C.; Nordlund, D.; Ho, K.-T.; Lien, D.-H.; Lin, C.-H.; Liang, R.-Z.; Miao, x. Extremely Reduced Dielectric Confinement in Two-Dimensional Hybrid Perovskites with Large Polar Organics. *Commun. Phys.* **2018**, *1*, 80.
(44) Passarelli, J. V.; Mauck, C. M.; Winslow, S. W.; Perkinson, C. F.; Bard, J. C.; Sai, H.; Williams, K. W.; Narayanan, A.; Fairfield, D. J.; Hendricks, M. P.; et al. Tunable Exciton Binding Energy in 2D Hybrid Layered Perovskites Through Donor-Acceptor Interactions within the Organic Layer. *Nat. Chem.* **2020**, *12*, 672−682.
(45) Hohenberg, P.; Kohn, W. Inhomogeneous Electron Gas. *Phys. Rev.* **1964**, *136*, B864.
(46) Hedin, L. New Method for Calculating the One-Particle Green's Function with Application to the Electron-Gas Problem. *Phys. Rev.* **1965**, *139*, A796.
(47) Strinati, G. Application of the Green's functions method to thestudy of the optical properties of semiconductors. *Riv. Nuovo Cim.* **1988**, *11*, 1−86.
(48) Hybertsen, M. S.; Louie, S. G. Electron Correlation in Semiconductors and Insulators: Band Gaps and Quasiparticle Energies. *Phys. Rev. B* **1986**, *34*, 5390.
(49) Rohlfing, M.; Louie, S. G. Electron-Hole Excitations in Semiconductors and Insulators. *Phys. Rev. Lett.* **1998**, *81*, 2312.
(50) Rohlfing, M.; Louie, S. G. Electron-Hole Excitations and Optical Spectra from First Principles. *Phys. Rev. B* **2000**, *62*, 4927.
(51) Qiu, D. Y.; da Jornada, F. H.; G, L. S. Optical Spectrum of MoS_2: Many-Body Effects and Diversity of Exciton States. *Phys. Rev. Lett.* **2013**, *111*, 216805.
(52) Refaely-Abramson, S.; Qiu, D. Y.; Louie, S. G.; Neaton, J. B. Defect-Induced Modification of Low-Lying Excitons and Valley Selectivity in Monolayer Transition Metal Dichalcogenides. *Phys. Rev. Lett.* **2018**, *121*, 167402.
(53) Arora, A.; Drüppel, M.; Schmidt, R.; Deilmann, T.; Schneider, R.; Molas, M. R.; Marauhn, P.; de Vasconcellos, S. M.; Potemski, M.; Rohlfing, M.; et al. Interlayer Excitons in a Bulk Van der Waals Semiconductor. *Nat. Commun.* **2017**, *8*, 639.

https://doi.org/10.1021/acs.nanolett.2c01306
Nano Lett. 2022, 22, 4870−4878

(54) Refaely-Abramson, S.; da Jornada, F. H.; Louie, S. G.; Neaton, J. B. Origin of Singlet Fission in Solid-Pentacenefrom ab initio Green's Function Approach. *Phys. Rev. Lett.* **2017**, *119*, 267401.
(55) Bokdam, M.; Sander, T.; Stroppa, A.; Picozzi, S.; Sarma, D. D.; Franchini, C.; Kresse, G. Role of Polar Phonons into the Photo-Excited State of Metal Halide Perovskites. *Sci. Rep.* **2016**, *6*, 28618.
(56) Umari, P.; Mosconi, E.; De Angelis, F. Infrared Dielectric Screening Determines the Low Exciton Binding Energy of Metal-Halide Perovskites. *J. Phys. Chem. Lett.* **2018**, *9*, 620−627.
(57) Biega, R.-I.; Filip, M. R.; Leppert, L.; Neaton, J. B. Chemically Localized Resonant Excitons in Silver-Pnictogen Halide Double Perovskites. *J. Phys. Chem. Lett.* **2021**, *12*, 2057−2063.
(58) Blancon, J.-C.; Tsai, H.; Nie, W.; Stoumpos, C. C.; Pedesseau, L.; Katan, C.; Kepenekian, M.; Soe, C. M. M.; Appavoo, K.; Sfeir, M. Y.; et al. Extremely Efficient Internal Exciton Dissociation Through Edge States in Layered 2D Perovskites. *Science* **2017**, *355*, 1288−1292.
(59) Blancon, J. C.; Stier, A. V.; Tsai, H.; Nie, W.; Stoumpos, C. C.; Traore, B.; Pedesseau, L.; Kepenekian, M.; Katsutani, F.; Noe, G. T.; et al. Scaling Law for Excitons in 2D Perovskite Quantum Wells. *Nat. Commun.* **2018**, *9*, 2254.
(60) Kamminga, M. E.; de Wijs, G. A.; Havenith, R. W. A.; Blake, G. R.; Palstra, T. T. M. The Role of Connectivity on Electronic Properties of Lead Iodide Perovskite-Derived Compounds. *Inorg. Chem.* **2017**, *56*, 8408−8414.
(61) Giorgi, G.; Yamashita, K.; Palummo, M. Nature of Electronic and Optical Excitations of Ruddlesden-Popper Hybrid Organic-Inorganic Perovskites: The Role of the Many-Body Interactions. *J. Phys. Chem. Lett.* **2018**, *9*, 5891−5896.
(62) Molina-Sanchez, A. Excitonic States in Semiconducting Two-Dimensional Perovskites. *ACS Appl. Energy Mater.* **2018**, *1*, 6361−6367.
(63) Cho, Y.; Berkelbach, T. C. Optical Properties of Layered Hybrid Organic-Inorganic Halide Perovskites: A Tight Binding GW-BSE Study. *J. Phys. Chem. Lett.* **2019**, *10*, 6189−6196.
(64) DeCrescent, R. A.; Venkatesan, N. R.; Dahlman, C. J.; Kennard, R. M.; Chabinyc, M. L.; Schuller, J. A. Optical Constants and Effective-Medium Origins of Large Optical Anisotropies in Layered Hybrid Organic/Inorganic Perovskites. *ACS Nano* **2019**, *13*, 10745−10753.
(65) Giannozzi, P.; et al. QUANTUM ESPRESSO: a modular and open-source software project for quantum simulations of materials. *J. Phys.: Condens. Matter.* **2009**, *21*, 395502.
(66) Giannozzi, P.; Andreussi, O.; Brumme, T.; Bunau, O.; Nardelli, M. B.; Calandra, M.; Car, R.; Cavazzoni, C.; Ceresoli, D.; Cococcioni, M.; et al. Advanced capabilities for materials modelling with Quantum ESPRESSO. *J. Phys.: Condens. Matter* **2017**, *29*, 465901.
(67) Perdew, J. P.; Burke, K.; Ernzerhof, M. Generalized Gradient Approximation Made Simple. *Phys Rev Lett* **1996**, *77* (18), 3865−3868.
(68) Deslippe, J.; Samsonidze, G.; Strubbe, D. A.; Jain, M.; Cohen, M. L.; Louie, S. G. BerkeleyGW: A massively parallel computer package for the calculation of the quasiparticle and optical properties of materials an nanostructures. *Comput. Phys. Commun.* **2012**, *183*, 1269−1289.
(69) Del Ben, M.; da Jornada, F. H.; Canning, A.; Wichmann, N.; Raman, K.; Sasanka, R.; Yang, C.; Louie, S. G.; Deslippe, J. Large-Scale GW Calculations on Pre-Exascale HPC Systemss. *Comput. Phys. Commun.* **2019**, *235*, 187−195.
(70) Ben, M.; Yang, C.; Li, Z.; da Jornada, F. H.; Louie, S. G.; Deslippe, J. Accelerating Large-Scale Excited-State GW calculations on Leadership HPC systems. *Proc. of the 2020 SC20: International Conference for High Performance Computing, Networking, Storage and Analysis (SC)* **2020**, *1*, 1−11.
(71) Filip, M. R.; Giustino, F. GW Quasiparticle Band Gap of the Hybrid Organic-Inorganic Perovskite $CH_3NH_3PbI_3$: Effect of Spin-Orbit Interaction, Semicore Electrons, and Self-Consistency. *Phys. Rev. B* **2014**, *90*, 245145.
(72) Brivio, F.; Butler, K. T.; Walsh, A.; van Schilfgaarde, M. Relativistic quasiparticle self-consistent electronic structure of hybrid halide perovskite photovoltaic absorbers. *Phys. Rev. B* **2014**, *89*, 155204.
(73) Scherpelz, P.; Govoni, M.; Hamada, I.; Galli, G. Implementation and Validation of Fully Relativistic GW Calculations: Spin-Orbit Coupling in Molecules, Nanocrystals, and Solids. *J. Chem. Thory Comput* **2016**, *12*, 3523−3544.
(74) Wiktor, J.; Rothlisberger, U.; Pasquarello, A. Predictive Determination of Band Gaps of Inorganic Halide Perovskites. *J. Phys. Chem. Lett.* **2017**, *8*, 5507−5512.
(75) Leppert, L.; Rangel, T.; Neaton, J. B. Towards predictive band gaps for halide perovskites: Lessons from one-shot and eigenvalue self-consistent GW. *Phys. Rev. Mater.* **2019**, *3*, 103803.
(76) Dyksik, M.; Duim, H.; Maude, D. K.; Baranowski, M. A.; Loi, M.; Plochocka, P. Brightening of dark excitons in 2D perovskites. *Sci. Adv.* **2021**, *7*, eabk0904.
(77) Fieramosca, A.; De Marco, L.; Passoni, M.; Polimeno, L.; Rizzo, A.; Rosa, B. L. T.; Cruciani, G.; Dominici, L.; De Giorgi, M.; Gigli, G.; et al. Tunable Out-of-Plane Excitons in 2D Single-Crystal Perovskites. *ACS Photon.* **2018**, *5*, 4179−4185.
(78) Walters, G.; Haerberle, L.; Quinteo-Bermudez, R.; Brodeur, J.; Kena-Cohen, S.; Sargent, E. H. Directional Light Emission from Layered Metal Halide Perovskite Crystals. *J. Phys. Chem. Lett.* **2020**, *11*, 3458−3465.
(79) Wannier, G. H. The Structure of Electronic Excitation Levels in Insulating Crystals. *Phys. Rev.* **1937**, *52*, 191.
(80) Wang, Y.; Song, F.; Yuan, Y.; Dang, J.; Xie, X.; Sun, S.; Yan, S.; Hou, Y.; Lou, Z.; Xu, X. Strong Triplet-Exciton-LO-Phonon Coupling in Two-Dimensional Layered Organic-Inorganic Hybrid Perovskite Single Crystal Microflakes. *J. Phys. Chem. Lett.* **2021**, *12*, 2133−2141.
(81) Luo, B.; Guo, Y.; Li, X.; Xiao, Y.; Huang, X.; Zhang, J. Z. Efficient Trap-Mediated Mn^{2+} Dopant Emission in Two Dimensional Single-Layered Perovskite $(CH_3CH_2NH_3)_2PbBr_4$. *J. Phys. Chem. C* **2019**, *123*, 14239−14245.
(82) Malcioglu, O. H.; Gebauer, R.; Rocca, D.; Baroni, S. turboTDDFT - A code for the simulation of molecular spectra using the Liouville-Lanczos approach to time-dependent density-functional perturbation theory. *Comput. Phys. Commun.* **2011**, *182*, 1744.
(83) Ge, X.; Binnie, S. J.; Rocca, D.; Gebauer, R.; Baroni, S. turboTDDFT 2.0-Hybrid functionals and new algorithms within time-dependent density-functional perturbation theory. *Comput. Phys. Commun.* **2014**, *185*, 2080.
(84) Adler, S. L. Quantum theory of the dielectric constant in real solids. *Phys. Rev.* **1962**, *126*, 413−420.
(85) Wiser, N. Dielectric constant with local field effects included. *Phys. Rev.* **1963**, *129*, 62−69.
(86) Ashcroft, N. W.; Mermin, N. D. *Solid State Physics*; Brooks/Cole: 1976.
(87) Cortecchia, D.; Mroz, W.; Neutzner, S.; Borzda, T.; Folpini, G.; Brescia, R.; Petrozza, A. Defect Engineering in 2D perovskite by Mn(II) Doping for Light-Emitting Applications. *Chem.* **2019**, *5*, 2146−2158.
(88) Knutson, J. L.; Martin, J. D.; Mitzi, D. B. Tuning the Band Gap in Hybrid Tin Iodide Perovskite Semiconductors Using Structural Templating. *Inorg. Chem.* **2005**, *44*, 4699−4705.
(89) Berger, R. F.; Fennie, C. J.; Neaton, J. B. Band Gap and Edge Engineering via Ferroic Distortion and Anisotropic Strain: The Case of SrTiO3. *Phys. Rev. Lett.* **2011**, *107*, 146804.
(90) Mao, L.; Ke, W.; Pedesseau, L.; Wu, Y.; Katan, C.; Even, J.; Wasielewski, M. R.; Stoumpos, C. C.; Kanatzidis, M. G. Hybrid Dion-Jacobson 2D Lead Iodide Perovskites. *J. Am. Chem. Soc.* **2018**, *140*, 3775−3783.
(91) Hamann, D. R. Optimized norm-conserving Vanderbilt pseudopotentials. *Physical Review B* **2013**, *88*, 085117.
(92) van Setten, M. J.; Giantomassi, M.; Bousquet, E.; Verstraete, M. J.; Hamann, D. R.; Gonze, X.; Rignanese, G.-M. The PseudoDojo: Training and Grading a 85 Element Optimized Norm-Conserving

https://doi.org/10.1021/acs.nanolett.2c01306
Nano Lett. 2022, 22, 4870−4878

Pseudopotential Table. *Computer Physics Communications* **2018**, *226*, 39−54.
(93) Godby, R. W.; Needs, R. Metal-Insulator Transition in Kohn-Sham Theory and Quasi- particle theory. *Phys. Rev. Lett.* **1989**, *62*, 1169.
(94) Deslippe, J.; Samsonidze, G.; Jain, M.; Cohen, M. L.; Louie, S. G. Coulomb-hole summations and energies for GW calculations with limited number of empty orbitals: A modified static remainder approach. *Phys. Rev. B* **2013**, *87*, 165124.
(95) Möller, C. K. Crystal Structure and Photoconductivity of Cæsium Plumbohalides. *Nature* **1958**, *182*, 1436.
(96) Zhao, L.; Lin, Y.-H. L.; Kim, H.; Giebink, N. C.; Rand, B. P. Donor/Acceptor Charge-Transfer States at Two-Dimensional Metal Halide Perovskite and Organic Semiconductor Interfaces. *ACS Energy Lett.* **2018**, *3*, 2708−2712.

https://doi.org/10.1021/acs.nanolett.2c01306
Nano Lett. 2022, 22, 4870−4878